Dalton Transactions

ROYAL SOCIETY OF CHEMISTRY

PAPER

View Article Online
View Journal | View Issue



Cite this: *Dalton Trans.*, 2022, **51**, 2827

# Erbium energy bridging upconversion mechanism studies on BAKL:$Er^{3+}$/$Yb^{3+}$ glass-ceramics and simultaneous enhancement of color purity of the green luminescence†

Prasenjit Prasad Sukul, *[a] Kaushal Kumar[b] and Hendrik Swart *[a]

Borate oxyfluoride glasses are transparent in the infrared, ultraviolet and visible regions and represent an ideal host matrix for optically active dopants. Due to their lower phonon energies compared to a silicate glass matrix, non-radiative transitions are suppressed and high luminescence efficiency is expected. This work reports on a complete upconversion (UC) luminescence study of the optically active $B_2O_3$–$Al_2O_3$–KF–LiO (BAKL) glass-ceramics incorporated with $Er^{3+}$/$Yb^{3+}$ ions. The triclinic BAKL:$Er^{3+}$/$Yb^{3+}$ glass-ceramic (GC) phosphor was synthesized using the conventional melt-quenching technique and the subsequent heat treatment of the precursor glass. The successful synthesis of BAKL:$Er^{3+}$/$Yb^{3+}$ GCs was confirmed by X-ray diffraction, Fourier transform infra-red and differential thermal analysis measurements. The glasses were crystallized under controlled conditions, and the influence of phase composition (glass-to-crystalline phase ratio) on the wavelength and UC luminescence was thoroughly studied under 980 nm excitation. Interesting color tuning properties (white to intense green emission) of the sample were observed with laser pump power increment. The color tuning properties were explained using a new strategy *i.e.* the energy bridging mechanism between $Er^{3+}$ ion clusters through an intermediate $Yb^{3+}$ level. Moreover, their high color purity is well retained by varying the NIR excitation pump power densities and photometric characterization indicated the suitability in light emitting diodes and $Er^{3+}$ doped fiber amplifier applications.

Received 19th November 2021,
Accepted 14th January 2022

DOI: 10.1039/d1dt03918k

rsc.li/dalton



## 1. Introduction

The past decades have witnessed the blossom of rare earth (RE) ion doped upconversion (UC) materials due to their vast practical applications in the field of solid state lasers, UC lasers, waveguide lasers, $Er^{3+}$-doped fiber amplifiers (EDFAs), light emitting diodes (LEDs), phosphor inkjet printing, luminescent solar concentrators and optical sensing.[1–5] Since RE-incorporated oxyfluoride glass-ceramics (OxGCs) were reported by Wang and Ohwaki,[6] these luminescent glass-ceramics (GCs) were widely researched in the past as a potential optical material. In the present day, the glass matrix is preferred over the crystalline matrix for lanthanide doping because of the ease of synthesis in different shapes and sizes with uniform distribution of RE ion concentration and is suitable for developing low-loss, high-strength and low-cost optical fibers. The oxyfluoride glasses could be thermally treated close to the crystallization temperature through controlled nucleation and transparent OxGCs can be achieved, in which fluoride crystallites are dispersed in the oxide glassy matrix. The successful incorporation of RE ions into the oxyfluoride matrix can provide a combinational advantage of the superior chemical and mechanical stability of oxide glasses and the low phonon energy environment of fluoride nanocrystals and thus they would exhibit excellent UC properties.[7–9]

The preferred mechanism involves formation as on heating at a suitable temperature, precursor glasses at first reach a metastable liquid state. Afterwards, the metastable liquid state overcomes a thermodynamic potential barrier to nucleate and eventually forms the famous glass-ceramics with lower free energy in which the segregated nanocrystals are lying homogeneously in the residual glassy phase.[10] The reason glass-ceramics remain highly transparent is due to the much smaller size of the precipitated nanocrystals than the wavelength of light in the visible and near-infrared region.[11,12] Another reason is due to weak absorption which occurs as a result of maximum disorderliness in the structure. In particular, RE

[a]*Department of Physics, University of Free State, Bloemfontein 9300, Republic of South Africa. E-mail: sukul.PP@ufs.ac.za, swartHC@ufs.ac.za*
[b]*Optical Materials & Bio-imaging Research Laboratory, Department of Physics, Indian Institute of Technology (ISM), Dhanbad 826004, India*

†Electronic supplementary information (ESI) available. See DOI: 10.1039/d1dt03918k

ions can enrich preferentially in the precipitated fluoride nanocrystals after crystallization and present excellent UC behaviour due to the reduced nonradiative relaxation and enhanced energy-transfer (ET) efficiency because of the shorter $RE^{3+}$–$RE^{3+}$ distance compared to that in the precursor glasses.[13]

Recently, OxGCs have been preferred over silicate GCs as they exhibit the features of both oxide and fluoride matrices such as ease of preparation, thermal stability and moisture resistance. They have low phonon energy characteristics that permit the fluorescence of a rare earth ion over a wide spectral region. Improvements are reported when the incorporation of boron ion as a glass former into the host matrix which increases the thermal stability (higher bond strength), and has a smaller cation size, valency of +3 and small heat of fusion, chemical durability and ease of fabrication at a lower melting temperature.[14] There are several reports on the advantages of selecting luminescent oxyfluoride glasses over aluminosilicate glasses.[7,15,16] Moreover, fluorozirconate GC composition, notably $ZrF_4$–$BaF_2$–$LaF_3$–$AlF_3$–NaF (ZBLAN), is one of the most stable systems against devitrification among fluoride glasses.[17] The structural properties of these conventional oxyfluoride borate GCs have been explored widely by researchers.[18,19] However, among the existing reported borate GCs, oxyfluoride boroaluminate GCs are seldom reported; however, they have a strong advantage in terms of their composition. Thus, we tried to shed some more light into this quaternary GC composition and chose $B_2O_3$–$Al_2O_3$–KF–LiO (BAKL) GCs, hoping that this could be used as an excellent luminescent host material. The contribution of $B_2O_3$ is to add maximum strength to the host and KF is added to give a low phonon environment to the material; in addition, $Al_2O_3$ works as a novel glass modifier and LiO works as a good binder and gives maximum strength to the material.[20,21] Therefore, keeping the above factors in mind, the present work is carried out to examine the role of an RE dopant on the structural and upconversion properties of BAKL GCs.

Trivalent erbium ($Er^{3+}$) is the most studied among RE ions because of its emission presence in the visible range, while its optical response is in the near-infrared (NIR) spectral region. Moreover, $Er^{3+}$ has a favorable energy level structure with two transitions ($^4I_{15/2} \rightarrow {}^4I_{11/2}$ and $^4I_{15/2} \rightarrow {}^4I_{9/2}$) that can be efficiently pumped with high-power semiconductor lasers, being able to yield blue, and especially green and red emissions. In our previous studies on $Er^{3+}$ doped phosphors, excellent green UC was achieved using a suitable combination of RE ions and especially $Yb^{3+}$ ions as the sensitizers along with $Er^{3+}$ as the activators.[5,22] However, most of the work reported so far is based on the quantitative discussion of $Er^{3+}$ doped borate or borosilicate GCs. The present study aims to determine the excitation pump power-dependent UC and photometric characterizations (correlated color temperature (CCT), color purity) in $Er^{3+}/Yb^{3+}$ codoped BAKL GCs. Dramatically enhanced color tunability of $Er^{3+}$ emissions, which is a very rare phenomenon, was observed in this case and is discussed in detail using a new UC mechanism strategy. To explain the significant population transfer on the $Er^{3+}$ levels, the population rate equation model was used. Moreover, the color tuning properties and the suitability of the current phosphor in display devices (white light source) were also explored for the BAKL:$Er^{3+}/Yb^{3+}$ GCs.

## 2. Experimental

### 2.1 Characterization techniques

The crystal structure of the GC865 sample was recorded using a Bruker D8 advanced X-ray diffraction (XRD) measuring instrument with Cu-Kα target radiation (1.5405 Å) over a wide range of Bragg angles $2\theta$ ($10° \leq 2\theta \leq 90°$) at a scanning rate of 3 deg per min. A field emission scanning electron microscope (FESEM) (Jeol JSM-7800F) was used for the energy dispersive X-ray spectroscopy (EDS) analysis. The differential thermal analysis of the as-synthesized PG sample was carried out using an STA 6000 analyzer, PerkinElmer, under a $N_2$ atmosphere at a heating rate of 15 K $min^{-1}$. The thermogravimetric analysis (TGA) was performed on a Stanton Redcroft DTA/TGA 1600 (Rheometric Scientific, Epsom, UK) with a dry nitrogen atmosphere flowing through the reference channel at a heating rate of 15 K $min^{-1}$. For fine measurement at higher temperatures, the sample and reference materials were kept in matched pairs of platinum–rhodium alloy crucibles. An infrared absorption spectrum was recorded on a Fourier transformed IR (FTIR) spectrometer (PerkinElmer, Spectrum RX I) with 1 $cm^{-1}$ resolution using a KBr pellet technique in the wavenumber range of 4000 to 400 $cm^{-1}$. The UV-vis NIR absorption spectrum was recorded in the diffuse reflectance mode using a Lambda 950, UV-VIS-NIR spectrophotometer (PerkinElmer). Room temperature UC luminescence studies were carried out using a compact spectrophotometer with a dual-mode F980, Edinburgh Instruments. The behaviour of UC emission intensity from the sample was also studied at varying pump powers (530 mW to 1100 mW).

## 3. Results and discussion

### 3.1 Materials and methods

One of the green synthetic techniques used for obtaining polycrystalline materials from solid chemicals is the solid-state reaction commonly known as the ceramic method. Solid state reaction involves very high temperature initiation to cause a chemical reaction from solid starting materials to form a new solid with a well-defined structure, such as ceramics. The simplicity and large-scale manufacturing are two advantages of the solid-state reaction approach in inorganic chemistry. Previous upconversion studies on lithium oxyfluroborate glass ceramic hosts[23,24] show that with proper stoichiometric composition and a combinational advantage of the glass former, a modifier and binder are needed for intense emission from borate hosts. Despite the recent progress, the improvement of the UC emission efficiency and the unique color tuning pro-

 

perties of oxyflouroborate glass ceramic phosphor is still inefficient. In this work, the glass composition was designed in such a way that the majority of the phase corresponded to borate. As borate glass ceramics based on submicrometer, spherical crystallites of β-$BaB_2O_4$ (BBO) demonstrated second harmonic generation to UV wavelengths,[25] it makes it perfect for a promising optically active host. The secondary phases of $Al_2O_3$ and LiO in the present GCs are just to provide a superior extended glassy network to which KF is added to combine the optical advantages of fluoride nanocrystals to establish a lower phonon energy environment. The unique stoichiometric composition of the present glass ceramic phosphor makes it a novel compound that has not been studied or reported previously.

The oxyfluoride boroaluminate GCs in the ultrafine powder form were prepared using a standard solid-state reaction route followed by a melt quenching technique. The chemical composition used for the synthesis of the initial glass batch was as follows (in mol%):

$$80B_2O_3–10Al_2O_3–5KF–2.5LiO–2Yb_2O_3–0.5Er_2O_3$$

High-purity (~99.99%) analytical reagent grade raw materials *i.e.* $B_2O_3$ (Merck chemicals), $Al_2O_3$ (Otto chemicals), KF (Otto, India), LiO (Merck, India), $Yb_2O_3$ (Sigma Aldrich, Germany) and $Er_2O_3$ (Sigma Aldrich, Germany) were used for the synthesis. The synthesis of glass-ceramics was carried out using a standard method for bulk crystallization of a glass host *via* a double-stage heat treatment. In the first step, the well-ground stoichiometric chemicals were mixed and melted in a standard alumina ceramic crucible at 1100 °C for 1 h under an air atmosphere. In the second step, the melt was poured and quenched onto a preheated brass mould and then pressed by another plate to form precursor glasses (PGs). The glass sample was cut and polished after being cooled down to room temperature using a stepdown heat treatment. Subsequently, the polished PG samples were inertially heat-treated for 2 h at 865 °C, chosen from the different thermal analysis (DTA) measurements, to form GC through crystallization, which was labelled as GC 865.

### 3.2 Structural investigations

**3.2.1 X-ray powder diffraction (XRD) study.** The crystalline nature of the BAKL glass-ceramics system with $Er^{3+}/Yb^{3+}$ incorporation was tested by XRD before annealing. The analysis shows that the PG samples were non-crystalline and have two halo characteristics in nature (not shown in the figure). The current borate glass matrix also shows amorphous halos like silicate and aluminate glass matrices, approx. 26 and 31 degrees 2 theta, respectively. These halos are related to the crystalline matrix; however, due to the distribution of the bond lengths and bond angles, this causes the broadening of the peaks to give the characteristic amorphous halo peak positions.

The diffraction pattern of the GC 865 sample was recorded after heat treatment at 865 °C for 2 h (subsequent cooling for 24 h), as confirmed from the DTA profile. The XRD pattern shown in Fig. 1 reveals the multicrystalline phase nature of the

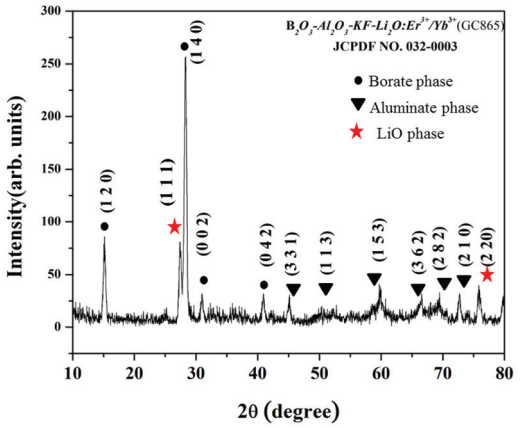


Fig. 1 Powder X-ray diffraction pattern of the $Er^{3+}/Yb^{3+}$ codoped BAKL glass ceramics (GC865) sample.

current GC865 phosphor. The most intense diffraction peaks are assigned due to $B_2O_3$ in the glassy network of the sample. As the majority of the stoichiometric composition is shared by $B_2O_3$ as the glass former, it is obvious to show maximum phase compositions by $B_2O_3$. Except for the $B_2O_3$ phase, the $Al_2O_3$ and LiO phases have also been confirmed and their corresponding miller indices are also assigned using a standard ICDD file (JCPDF no. 032-0003). To index the powder diffraction patterns, we used the Dicvol method[14] and a grid search indexing program.

For better structural information, the Rietveld refinement approach was used to examine the diffraction patterns using the Full Prof Suite software (free version). The refinement results obtained are shown in Fig. 2. The Rietveld refinement was performed using $AlB_2Li_3O_6$ as the standard model. The Rietveld refined result of the GC865 sample (with lattice parameters $a$ = 4.875889 Å, $b$ = 6.205774 Å, $c$ = 7.829860 Å and $V$ = 236.93 (Å$^3$) revealed that the samples crystallized in the triclinic phase with the space group $P\bar{1}$. In the refinement process, intermediate phases were also considered. Except for

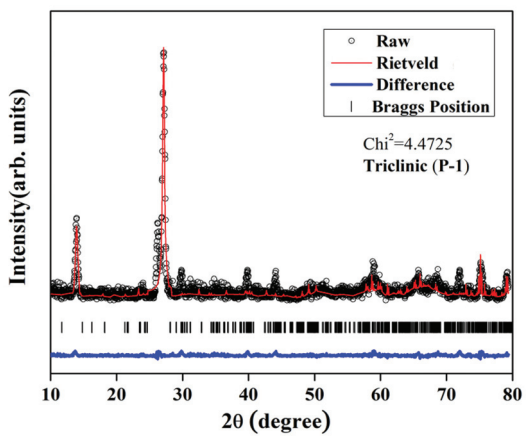


Fig. 2 Multiphase Rietveld refinement results for the BAKL:$Er^{3+}/Yb^{3+}$ (GC865) sample.

the triclinic $B_2O_3$ phase (major contributor), other phases, *e.g.* orthorhombic $Al_2O_3$ and monoclinic LiO also contributed, although the KF phase contribution is not observed in the present case. However, the positions of the dopant ions ($Er^{3+}$/$Yb^{3+}$) cannot be directly obtained through refinement; the probable locations in the crystal structure can still be inferred. The $B^{3+}$ ions are the most likely cations to be replaced by $Er^{3+}$. The difference curve between the observed and computed curves showed that they were well fitted. In this system, $B_2O_3$ acts as a glass former; however, it is seen from the diffraction pattern that $B_2O_3$ is also crystallized. Isabella *et al.*[26] have shown that in a $Bi_2O_3$–$B_2O_3$ system, the devitrification temperature is as low as 450/650 °C. In the present case, the sample was annealed at above 800 °C and because of this high temperature, $B_2O_3$ was also crystallized. The crystallization of the aluminum oxide-based borate glassy matrix with RE is an added advantage for exhibiting high nonlinear optical effects.[26,27]

To support the idea of the majority phase formation of $B_2O_3$, which is observed from the XRD patterns, EDS of the sample was done as shown in the ESI (Fig. ESI 1†). The expected metal ratio after the phosphor synthesis remained the same within the experimental error as the stoichiometric composition used during the synthesis which is confirmed from the different elemental mapping through EDS analysis (Fig. ESI 2†). Due to the EDS instrument limitation which has a beryllium window, only elements with a higher atomic number than beryllium could be detected. Therefore, the lithium element was not detected in the mapping process. The Li-percentage was confirmed in other characterization techniques used in this work, which can be found below.

**3.2.2 Differential thermal analysis (DTA).** Differential thermal analysis (DTA) is one of the important techniques to determine the crystallisation and phase transition temperatures of a glass-ceramic matrix. Depending upon the endothermic or exothermic peak positions, one can access the crystallisation of the ceramic from its alternative glassy phase. The DTA spectrum of the BAKL:$Er^{3+}$/$Yb^{3+}$ sample is shown in Fig. 3. The transition temperature and the melting temperature of this glass are 649 °C and 972 °C, respectively. Except for these, two extra exothermic peaks were observed at around 865 °C and 940 °C, respectively. The 940 °C point is the beginning of the melting temperature point. There is an obvious crystallization peak at 865 °C ($T_x$). The difference between the glass transition temperature ($T_g$) and the onset crystallization temperature ($T_x$), $\Delta T = T_x - T_g$, has been frequently quoted as a rough indicator of the glass's stability against crystallization.[28] It is desirable for a glass host to have a $\Delta T$ as large as possible. Here, the $\Delta T$ value is 107 °C ($\Delta T = T_x - T_g$ = 972–865 = 107 °C) which indicates that the $Er^{3+}$/$Yb^{3+}$ doped BAKL GCs have a fairly good thermal stability and are suitable for performing fabrication and capable of showing high UC luminescence.

Unfortunately, combined DTA/TGA measurements were not possible due to instrumental errors. We have explored the thermogravimetric analysis (TGA) on another instrument to check any weight loss that may occur during phase melting and crystallization along with the DTA profile. The TGA profile is shown in Fig. ESI 3 (refer to the ESI†). Moreover, the recorded TGA profile shows a 20–25% weight loss associated with this moisture loss indicating that the glass ceramics had absorbed a significant amount of atmospheric water prior to analysis. This can be explained by two probable incidents—one is that borate glass ceramic matrices are highly porous in nature and belong to the group of "thirsty glass"[29] because of their affinity to moisture. The other probable reason is that the TGA measurement is not done using the same instruments and also in the same time interval. As the TGA measurements were done later, the probability of moisture incorporation can be a possible reason to explain the current behaviour.

**3.2.3 Fourier transform infrared analysis (FTIR).** A detailed confirmation of the sample's growth is obtained by identifying the vibrational frequency of the host which regulates the overall UC emission. The FTIR spectrum of the sample in the range 2500–400 $cm^{-1}$ is shown in Fig. 4. The absorption peaks of the GC sample are assigned in the figure and the small presence of organic impurities was detected. Diffused absorption bands in the range 2340–2365 $cm^{-1}$ were observed and the doublet splitting was attributed to the –OH bonding vibrations that are formed at the non-bridging oxygen sites, commonly found in the borate glass matrix. The presence of –OH groups

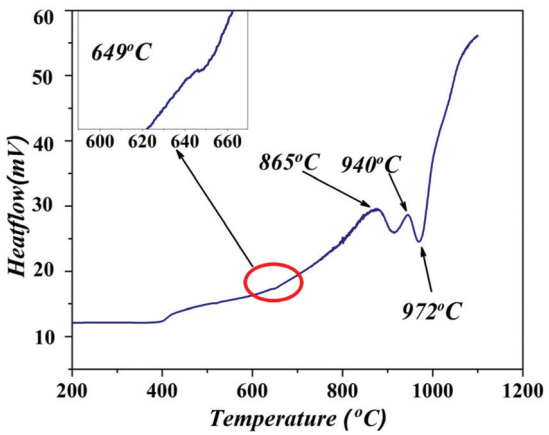


Fig. 3 DTA profile of the prepared glass at a heating rate of 15 K $min^{-1}$.

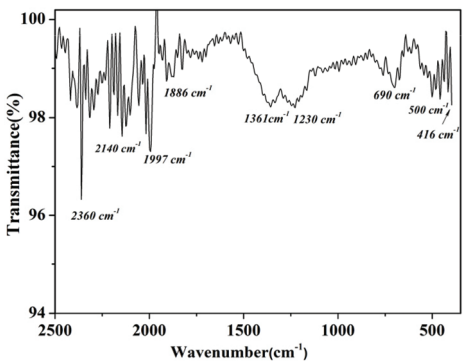


Fig. 4 FTIR spectra of the sample of $Er^{3+}$/$Yb^{3+}$ codoped BAKL GCs.

may be due to the KBr pellet technique used to record the IR spectra. The bands observed in the range 1230–1739 $cm^{-1}$ are attributed to the asymmetric stretching relaxation of the B–O bonds of trigonal $BO_3$ units. Similar types of vibrational modes were observed within 1200–1750 $cm^{-1}$.[27,30] This band was present due to the diborate linkage (B–O–B) in the borate glassy network. In this linkage, both boron atoms are tetrahedrally coordinated with triborate super structural units.[31,32]

However, the present sample does not show an absorption peak at 806 $cm^{-1}$ which confirms the absence of the boroxol ring in the glassy network. Moreover, low-frequency bands are observed at 690 $cm^{-1}$ which are assigned to the vibration of the metal cations ($Li^{2+}$) present in the sample. The absorption bands at 500 $cm^{-1}$ and 416 $cm^{-1}$ were presently associated with the fundamental mode of KF.[33] The cut-off phonon frequency of the sample is obtained at 416 $cm^{-1}$ which is low enough to observe the UC emission.

### 3.3 Optical emission studies

**3.3.1 UV-Vis spectroscopy.** To observe the possible excitation wavelengths of the current phosphor sample, we have used UV-vis spectroscopy. The UV-vis spectrum of the $Er^{3+}$/$Yb^{3+}$ codoped BAKL glass-ceramic powder was recorded against a reference standard $BaSO_4$ compound in the diffuse reflectance (DRS) mode. The UV-vis spectroscopy revealed bands at 380, 489, 525, 656, and 979 nm (Fig. 5). The sharp intense band at around 525 nm is due to the $^4H_{11/2} \leftarrow {}^4I_{15/2}$ absorption in the Er-ion.

The absorption bands at 380, 489, and 656 nm are the transitions from the $^4G_{11/2} \leftarrow {}^4I_{15/2}$, $^4F_{7/2} \leftarrow {}^4I_{15/2}$ and $^4F_{9/2} \leftarrow {}^4I_{15/2}$ in the Er-ion whereas the absorption bands at 979 nm are the result from the transitions $^2F_{7/2} \rightarrow {}^2F_{5/2}$ in the Yb-ion. It is to be mentioned that the existing broadband around 200 nm is due to the possible host absorption.

**3.3.2 Upconversion luminescence studies.** The UC emission spectra of $Er^{3+}$/$Yb^{3+}$ codoped BAKL GCs under 980 nm laser diode excitation were plotted and convoluted using a Gaussian fit with values ($chi^2$ = 0.9739 and 0.8896) (ESI†). The spectra comprise blue, green and red UC emission bands centred at 479, 525, 555 and 656 nm which correspond to the $^4F_{7/2} \rightarrow {}^4I_{15/2}$, $^2H_{11/2} \rightarrow {}^4I_{15/2}$, $^4S_{3/2} \rightarrow {}^4I_{15/2}$ and $^4F_{9/2} \rightarrow {}^4I_{15/2}$ transitions of the $Er^{3+}$ ion, respectively. The UC emission spectrum is showing broad emission in the green region; therefore, there was a need to convolute the spectra (Fig. ESI 4, ESI†). The reason for this kind of behaviour can be attributed to the fact that the $Er^{3+}$ ion may replace the cationic $B^+$ ion which is in a di-borate linkage (B–O–B) in the borate glassy network. As a result, the local symmetry of the host matrix is disturbed and as a consequence of the asymmetric phase site contribution, $Er^{3+}$ emission is more broadened than the conventional characteristic emission. Moreover, the emission peaks contain multiplet transitions due to which more than one peak can be seen with closely spaced energy levels ($\Delta E \sim 10$ $cm^{-1}$) of $Er^{3+}$. The multiplet transitions could be more carefully observed by doing low-temperature upconversion measurement (below 77 K). Due to the unavailability of the referred measurement technique in our laboratory, further exploration of the fine structure has not been reported. The UC measurements under different excitation pump power densities are plotted in the scanning range 400–700 nm as shown in Fig. 6(a). The insets of Fig. 6(a) show the photographs of the different colors emitted directly from the sample with different exciting powers. It is worth mentioning that the observable green emission was the most intense and at higher pump power dominated the red emission.

Conventionally, $Er^{3+}$ shows intense red emission in comparison to the characteristic green emission, when the dopant concentration of $Yb^{3+}$ < 8 mol%.[34] However, in this work, the $Yb^{3+}$ and $Er^{3+}$ concentrations were kept at 2.0 and 0.5 mol%, respectively, to get the optimum green luminescence. The optimization of the RE concentrations was already discussed in our earlier results.[5,35] Moreover, the intensities of the blue, green and red emissions were enhanced with the increase in the excitation pump power density. If a closer observation is made, it can be seen that the green emission is significantly improved rather than the improvement ratios of blue and red

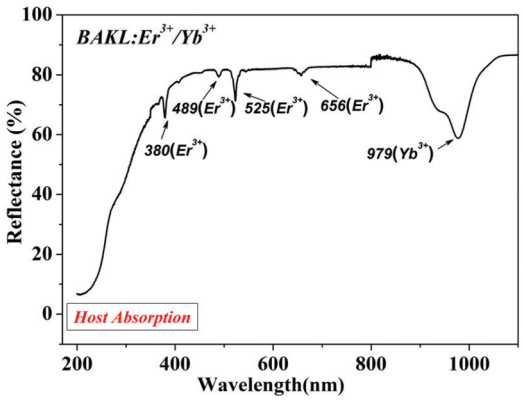


Fig. 5 The absorption spectra in the diffuse reflectance mode of the GC865 phosphor.

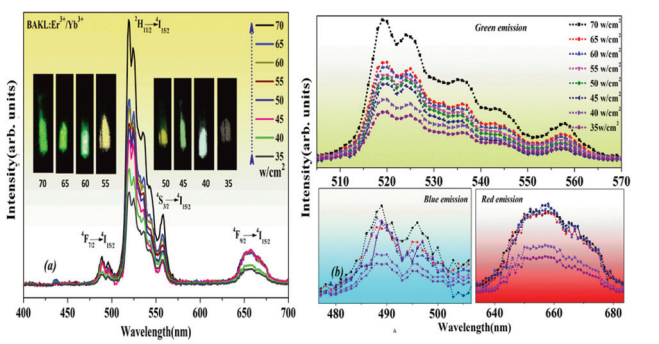


Fig. 6 (a) Variation of UC emission intensity with different input excitation powers of $Er^{3+}$/$Yb^{3+}$ doped BAKL using a 980 nm laser. (b) Variation of green, blue and red emission bands with different input excitation powers.

emissions. The specific scanning range 500–570 nm of the UC spectra where the green is intense is shown in Fig. 6(b).

The insets of Fig. 6(b) show the different emission regions with varying excitation pump power densities. This anomalous photometric behavior is explained using a new strategic UC mechanism that includes different photon processes (ESA, ET *etc.*) and is described in the following parts. The green ($I_G$) to red ($I_R$) and green ($I_G$) to blue ($I_B$) intensity ratios are plotted in Fig. 7(a) and (b), respectively, and the graphs also show that the $I_G/I_R$ ratio shows an exponential increase while the $I_G/I_B$ ratio shows a linear increase. The results also implicate that at a higher pump power, the green emission dominates the other visible emissions.

In general, the conversion of the IR emission to the visible emission can be ascribed to a multi-photon absorption process. The emission intensity variation with excitation pump power density in low power approximation will give a clear understanding of the UC process for the current GC865 phosphor. The following relation is

$$I_{UC} = P^n \quad (1)$$

Here, $n$ is the number of IR photons that must be absorbed for the emission. Moreover, a double logarithmic plot of the intensity and pump power yields a straight line with a slope that gives the nature of the UC, *i.e.*, the number of photons ($n$) absorbed in the UC process.[36]

The slopes of the double logarithmic plot almost show straight lines with $n$ values 1.13 + 0.01, 1.47 + 0.02 and 1.28 + 0.02 corresponding to emission peaks at 489 nm ($^4F_{7/2} \rightarrow {}^4I_{15/2}$), 525 nm ($^2H_{11/2} \rightarrow {}^4I_{15/2}$) and 656 nm ($^4F_{9/2} \rightarrow {}^4I_{15/2}$), respectively, as shown in Fig. 8. The current UC process relies on a two-photon absorption mechanism which could be confirmed by the approximate slope values ($n \sim 2$) observed from the plotted curves. But out of curiosity, we have investigated more to find the actual reason for the slope values which are near ($n \sim 2$) but not exactly 2. One possible explanation is that the absorption cross-section between $^2F_{7/2}$ ($Yb^{3+}$) and $^2F_{5/2}$ ($Yb^{3+}$) increases monotonically with temperature.[37] A similar observation of the $Yb^{3+}/Tb^{3+}$ codoped fluoroindate glass matrix was reported by Menezes *et al.*, where at a high temperature more high-frequency phonons participate in the non-resonant

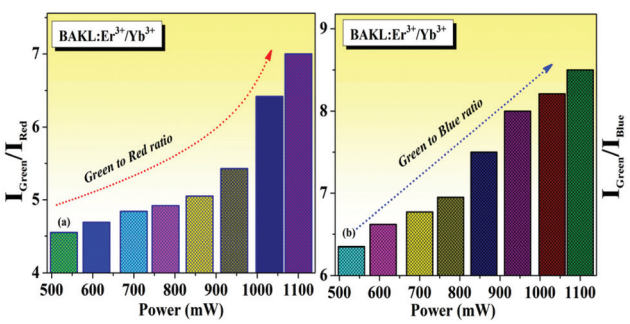


Fig. 7 (a) Green to red emission ratios with increasing pump power; (b) green to blue emission ratios with increasing pump power.

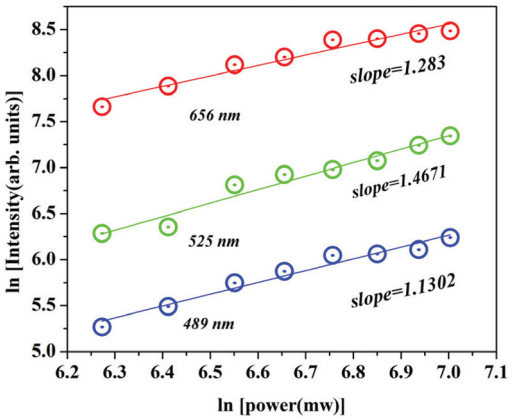


Fig. 8 Double logarithmic plot of pump power density *vs.* emission intensity for the GC865 sample.

energy transfer from $Yb^{3+}$ to $Ho^{3+}$. The present $Er^{3+}/Yb^{3+}$codoped matrix may be justified in a similar way. As a result of the local temperature increase, $Yb^{3+}$ and $Er^{3+}$ are excited more and more efficiently. Another possible explanation is that the multiphonon relaxation rate is also enhanced at high temperatures according to the following formula[37]

$$W_i^{NR}(T) = W_i^{NR}(T_0)\left[\frac{1-\exp(\hbar w/kT)}{1-\exp(\hbar w/kT_0)}\right]^{-q_i} \quad (2)$$

where $W_i^{NR}(T)$ is the temperature-dependent nonradiative decay rate and $q_i$ represents the number of phonons involved in the relaxation of level $i$ to the closest low energy level. Both processes exist side by side and compete with one another. Finally, fluorescence quenching is observed.

It is worth mentioning that we have used an optical chopper at a threshold frequency to avoid any direct heating in the sample while irradiating with a 980 nm laser at different pump power densities. However, it has been observed that the slope values are near 2 but not exactly 2. This leads us to reinvestigate the actual pump power dependence due to the temperature-dependent non-radiative decay. In practice, the actual emission intensity measured during pump power dependence can be written in the following form,

$$I_{observed} = I_{actual} - W_i^{NR} \quad (3)$$

To calculate the contribution of the temperature-dependent part, we have measured the local temperature of the sample using a K-type thermocouple placed near the sample chamber. At different pump powers, the local temperature is measured and represented as ($T$) and the room temperature is considered as ($T_0$). Incorporating the temperature-dependent term, we have again plotted the double logarithmic nature of pump power density *vs.* emission intensity, which is shown in Fig. 9. In the equations, we have considered $W_i^{NR}(T_0) = 50\,000$ $s^{-1}$;[37] at room temperature, $q_i$ is taken as 4 for the $^2H_{11/2}$ level ($Er^{3+}$), 6 for the $^4F_{7/2}$ level ($Er^{3+}$) and 6 for the $^2H_{11/2}$ level ($Er^{3+}$).[38] Fig. 9 shows the comparison between the observed

 

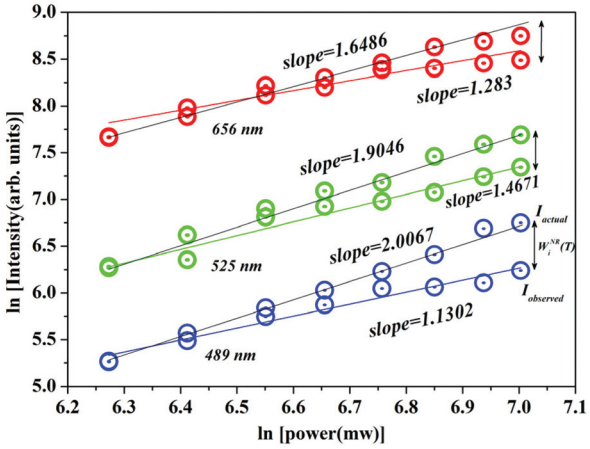


Fig. 9 Comparison of the double logarithmic plot of pump power density *vs.* emission intensity, incorporating the thermal quenching phenomena.

emission intensity at different pump powers *vs.* actual emission intensity incorporating the thermal quenching phenomena. It is found that due to thermal quenching, the observed slopes are showing (>2) values and after incorporating, the non-radiative rate is near 2 values. Therefore, we can conclude that due to irradiation by a 980 nm diode laser at different pump powers, in the sample the local temperature rises due to which the observed emission intensity is always less than the actual.

Based on the above confirmation, a suitable energy level diagram is drawn and the possible UC mechanisms are proposed.

**3.3.3 Rate-equation modelling.** The energy level diagram of an $Er^{3+}$–$Yb^{3+}$ codoped system including the $K$ and $C$ coefficients is shown in Fig. 10. It is well known that $Er^{3+}$ ions have a considerably more intricate energy level structure, although the upper levels are not significantly populated due to their high phonon energies.[39] In the synthesized GC865 sample, the $Er^{3+}$ to $Yb^{3+}$ concentration ratio was 1 : 4. Due to the significantly higher absorption cross-section (7 times) of $Yb^{3+}$ compared to that of $Er^{3+}$ at 980 nm excitation wavelength, it is much more plausible to discuss energy transfer from $Yb^{3+}$ to $Er^{3+}$.

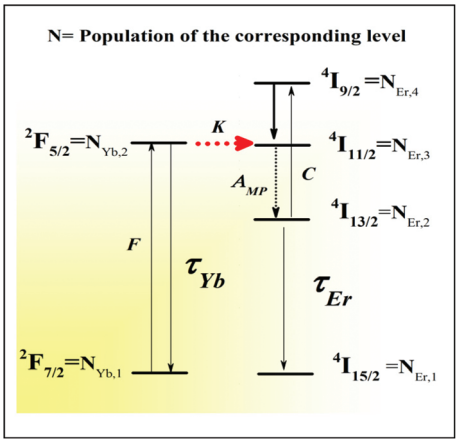


Fig. 10 Schematic energy-level diagram of Er–Yb with energy transfer ($K$) from $Yb^{3+}$ to $Er^{3+}$, upconversion ($C$) and radiative ($\tau$), and nonradiative ($A_{MP}$) energy relaxation.

The $Yb^{3+}$ ions absorb the NIR pump photon, and the stored energy is released either by spontaneous emission to the ground state or through energy transfer ($K$) to the $Er^{3+}$ ions. The energy in $^4I_{11/2}$ relaxes to the lower $Er^{3+}$ energy level $^4I_{13/2}$ *via* a rapid non-radiative process called $A_{MP}$; because of the short decay, the back transfer to the $Yb^{3+}$ ion is minimal in this fluoride glass ceramic with a high phonon energy. $^4I_{13/2}$ decays spontaneously to the ground level or empties *via* a cooperative UC process ($C$).[22]

For a better understanding of the power-dependent anomalous behaviour, a theoretical description has been given based on the steady-state rate equations for the $Er^{3+}$ and $Yb^{3+}$ co-doped systems. The possible three energy transfer upconversion (ETU) processes from $Yb^{3+}$ to $Er^{3+}$ are (refer to Fig. 10 & 11).

**ETU 1:** $^2F_{5/2}$ ($Yb^{3+}$) + $^4I_{15/2}$ ($Er^{3+}$) → $^2F_{7/2}$ ($Yb^{3+}$) + $^4I_{11/2}$ ($Er^{3+}$)

**ETU 2:** $^2F_{5/2}$ ($Yb^{3+}$) + $^4I_{11/2}$ ($Er^{3+}$) → $^2F_{7/2}$ ($Yb^{3+}$) + $^4F_{7/2}$ ($Er^{3+}$)

**ETU 3:** $^2F_{5/2}$ ($Yb^{3+}$) + $^4I_{13/2}$ ($Er^{3+}$) → $^2F_{7/2}$ ($Yb^{3+}$) + $^4F_{9/2}$ ($Er^{3+}$)

The $Er^{3+}$ ions increased to the $^4F_{7/2}$ level by ETU-2 and relaxes nonradiatively to the $^2H_{11/2}$/$^4S_{3/2}$ levels, and subsequently, radiative transition to the ground state ($^4I_{15/2}$) yields the characteristic green (525/555 nm) emission bands. The population increment of the $^4I_{13/2}$ level of $Er^{3+}$ can be explained using the two basic mechanisms followed here: (i) energy back-transfer: $^2H_{11/2}$/$^4S_{3/2}$ ($Er^{3+}$) + $^2F_{7/2}$ ($Yb^{3+}$) → $^4F_{13/2}$ ($Er^{3+}$) + $^2F_{5/2}$ ($Yb^{3+}$) and (ii) the cross-relaxation process of $Er^{3+}$ ions: $^2H_{11/2}$/$^4S_{3/2}$ + $^4I_{15/2}$ → $^4I_{9/2}$ + $^4I_{13/2}$.

If we took a closer observation, the ETU 2 process is found to be more significant due to its energy level matching profile. Therefore, considering that maximum energy transfer can happen through $Yb^{3+}$ to $Er^{3+}$ using the ETU2 process, a theoretical model is established here. The model consists of 5 rate equations for the populations of the primary energy levels of $Er^{3+}$, considering the main energy transfer mitigation processes as per the discussion made in the $Er^{3+}$–$Yb^{3+}$ co-doped system. The solutions of these rate equations will provide the information on whether energy back transfer will occur or cross relaxation will prevail.[40] For simplification, we can consider these rate equations are analogues to a four-level laser system. We have $N_{Yb,1}$ at the ground level and the pumping process excites the atoms from $^2F_{7/2}$ to $^2F_{5/2}$ of $Yb^{3+}$ ions; the pumping rate is F. Atoms at the $^2F_{5/2}$ level have longer decay than those at the $^2F_{7/2}$ level; the decay time is $\tau_{Yb}$. As the $^2F_{5/2}$ level of the $Yb^{3+}$ ions and the $^4I_{11/2}$ level of $Er^{3+}$ ions are at the same energy level, energy transfer from $Yb^{3+}$ to $Er^{3+}$ occurs. Now, the population at the $^4I_{11/2}$ level (shorter decay) shifts to a lower level to the $^4I_{13/2}$ level *via* a nonradiative transition $A_{MP}$. As the $^4I_{13/2}$ level of $Er^{3+}$ ions is a metastable state, the following multiple ESA transitions contribute to the population of the higher $Er^{3+}$ energy level. In this case, the total $Yb^{3+}$ population is given by $N_{Yb} = N_{Yb,2} + N_{Yb,1}$ and the total $Er^{3+}$ popu-

lation is given by $N_{Er} = N_{Er,4} + N_{Er,3} + N_{Er,2} + N_{Er,1}$. Then, we have the rate equations for the four-level laser systems:

$$\frac{dN_{Yb,2}}{dt} = \sigma_{abs,Yb}N_{Yb,1}F - KN_{Yb,2}N_{Er,1} - \frac{N_{Yb,2}}{\tau_{Yb}} + \sigma_{abs,Er}N_{Yb,1} \quad (4)$$

$$\frac{dN_{Er,2}}{dt} = N_{Er,3}A_{3-2}^{MP} - \frac{N_{Er,2}}{\tau_{Er,2-1}} - 2CN_{Er,2}^{2} + KN_{Er,3} \quad (5)$$

$$\frac{dN_{Er,3}}{dt} = KN_{Yb,2}N_{Er,1} - N_{Er,4}A_{4-3}^{MP} - N_{Er,3}A_{3-2}^{MP} \quad (6)$$

$$\frac{dN_{Er,4}}{dt} = CN_{Er,2}^{2} - N_{Er,4}A_{4-3}^{MP} \quad (7)$$

In the above equations, $N_{Er,i}$ ($i$ = 1, 2, 3, and 4) are the population densities of the $^4I_{15/2}$, $^4I_{13/2}$, $^4I_{11/2}$ and $^4I_{9/2}$ levels of $Er^{3+}$, respectively. $N_{Yb,i}$ ($i$ = 0 and 1) are the population densities of the $^2F_{7/2}$ and $^2F_{5/2}$ levels, respectively, of $Yb^{3+}$. $\sigma_{abs,Er}$ and $\sigma_{abs,Yb}$ are the absorption cross-sections of $Er^{3+}$ and $Yb^{3+}$, respectively. $F$ is the excitation pump rate, $A_{MP}$ is the multi-phonon decay rate, $\tau_{Yb}$ = 1.6 ms is the lifetime of the $Yb^{3+}$ ions without $Er^{3+}$ co-doping and $\tau_{Er,2}$ = 10 ms is the lifetime of the $Er^{3+}$ ions to the ground state.[39] Eqn (4) represents the rate of the population densities at the $^2F_{5/2}$ level of $Yb^{3+}$ which depends on the absorption coefficient and population density of the $^2F_{7/2}$ level of $Yb^{3+}$. Eqn (5) represents the rate of population densities at the $^4I_{13/2}$ level of $Er^{3+}$ which depends on the contribution of non-radiative ($A_{MP}$) transition between the levels (3 → 2) of $Er^{3+}$. Eqn (6) represents the rate of population of the $^4I_{11/2}$ level of $Er^{3+}$, which depends on the energy transfer factor ($K$) and the population of the $^2F_{5/2}$ level of $Yb^{3+}$. Moreover, the rate of population at the $^4I_{9/2}$ level is given by eqn (7) which depends on the square of the population at the $^4I_{13/2}$ level of the $Er^{3+}$.

The relaxation rates can be calculated using the equation,[41]

$$A_{MP}(\Delta E) = A_{MP}(0)\exp\left[-\frac{\Delta E}{\hbar\omega}\left(\ln\frac{\Delta E}{\hbar\omega g} - 1\right)\right] \quad (8)$$

where $\Delta E$ is the energy gap between the $^4I_{11/2}$ and $^4I_{13/2}$ levels, $h\nu$ is the maximum phonon energy of the host, and $g = 9 \times 10^3$ is the electron–phonon coupling strength. We can calculate the values using the Jablonski energy level diagram for $Er^{3+}$ ion—$\Delta E \approx 3680\ cm^{-1}$, $h\nu \approx 1200\ cm^{-1}$, and $A_{MP}(0) \approx 10^{11}\ s^{-1}$,[41] and the decay time is 28 $\mu s^{-1}$. The population at the $^4I_{11/2}$ energy level is found to be negligible in this case due to the rapid relaxation rates. As the pump power increases from low to high density, the population at the higher energy level becomes independent of the pump power, which means that the energy transfer process becomes highly efficient at high power densities. The above equations also provide important insights into the further mechanism occurring in between the $Er^{3+}$ energy levels (after the 1st energy transfer from $^2F_{5/2}$ to $^4I_{11/2}$ level). By solving these equations, it can be predicted whether energy back-transfer and cross-relaxation processes will become much more efficient at high pump powers to saturate the $^4I_{13/2}$ level and that the power dependence of the red emitting level $^4F_{9/2}$ will be reduced or not. The unknown constants $K$ and $C$ can be obtained by observing the time-dependent lifetime decay curves of the $Er^{3+}$ emitting levels. Moreover, the typical values of energy transfer ($K$) are found to be in the order of $4 \times 10^{-17}\ cm^3\ s^{-1}$ ($^2F_{5/2} \rightarrow {}^4I_{11/2}$) and the cooperative upconversion emission value ($C$) is found to be $4 \times 10^{-18}\ cm^3\ s^{-1}$ for $Er^{3+}/Yb^{3+}$ co-doped borate-silicate glass reported by Shanfeng *et al.*[37] This interpretation matches the experimental results shown in Fig. 11 and explains the anomalous power-dependent behavior mentioned above.

As we discussed, the probability of the ET phenomena is more likely to happen in an $Er^{3+}$–$Yb^{3+}$ codoped system due to a larger absorption coefficient which simultaneously lowers the probability of direct absorption of the NIR photon in the $Er^{3+}$ ions at the ground level through the ground-state absorption (GSA) process. The schematic energy level diagram of the $Er^{3+}/Yb^{3+}$ ions with possible pathways defining UC is shown in Fig. 11. The significant population increase at the $^4I_{11/2}$ level is considered only by efficient ET from the $Yb^{3+}$ to $Er^{3+}$. However, the second NIR photon is again absorbed from the $^4I_{11/2}$ level as it is a metastable state and *via* the excited state absorption (ESA) process it populates at the $^4F_{7/2}$ level. Here, a part of the $Er^{3+}$ energy decays nonradiative at the $^4I_{13/2}$ level and the rest populate the $^4F_{9/2}$ level by absorbing the second NIR photon through another ESA. Moreover, the ions from the $^4F_{7/2}$ level decay nonradiatively to the lower-lying $^2H_{11/2}$ and $^4S_{3/2}$ manifold *via* the possible emission of 4 and 6 phonons, respectively.[38] Since the energy gap between the $^2H_{11/2}$ and $^4F_{7/2}$ levels is 2600 $cm^{-1}$ while it is around 3000 $cm^{-1}$ between the $^4S_{3/2}$ and $^4F_{7/2}$ levels, it justifies the behaviour. Finally, the ions from the $^2H_{11/2}$ and $^4S_{3/2}$ manifold relax radiatively to the ground level leading to green emissions of about 525 nm and 545 nm, respectively. Now the $Er^{3+}$ ions in the $^4F_{9/2}$ state relax to the ground state producing red emission about 656 nm corresponding to the $^4F_{9/2} \rightarrow {}^4I_{15/2}$ transition. The possible mechanism for the blue emission is by populating the $^4F_{7/2}$ level. The $Yb^{3+}$ ions in $^2F_{7/2}$ (ground state) were excited to the $^2F_{5/2}$ state, and then transfer their energy to the nearest energy level of $Er^{3+}$ *i.e.* $^4I_{11/2}$ level. The level $^4I_{11/2}$ readily transfers the whole energy to the nearest $^4F_{7/2}$ level of $Er^{3+}$ and also from

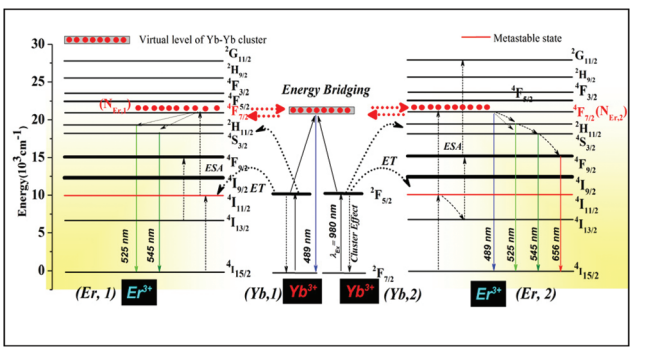


Fig. 11 A schematic energy level diagram of the $Er^{3+}/Yb^{3+}$ ions with possible pathways defining upconversion.

the $^2F_{5/2}$ level of the sensitizer $Yb^{3+}$ there is an extra energy transfer that happens to the $^4F_{7/2}$ level which is the cause of significant population in the following level. Finally, the $^4F_{7/2}$ level radiatively relaxes to the $^4I_{15/2}$, resulting in blue emission centred at 489 nm. In addition, it is supposed that due to the inhomogeneity in the sample there is a chance to form Yb ion clusters and these clusters cooperatively emit at 489 nm.[5,42,43] Here, simultaneous excitation of a pair of $Yb^{3+}$ ions accompanied by an energy transition to the $^4F_{7/2}$ level of the $Er^{3+}$ ions and the emission of a single visible photon in the following manner: $Yb^{3+}$ ($^2F_{5/2}$) + $Yb^{3+}$ ($^2F_{5/2}$) = $Yb^{3+}$ ($^2F_{7/2}$) + $h\gamma$, where the photon energy of the cooperative emission is almost exactly twice the energy of the normal (single-ion) fluorescence. This behaviour can most likely be attributed to the non-resonance energy transfer. Here, the possibility of blue emission (489 nm) is supposed from the cooperative emission of the $Yb^{3+}$ ion.[5]

**3.3.4 Phenomena of energy bridging through Er–Er ion clustering.** The anomalous behaviour observed in the pump power–dependent upconversion emission studies can be explained by another possible mechanism. The GC865 sample shows efficient color tuning from white to intense green emission for a moderate low to a high pump power density. At a moderate low pump power, the UC mechanism explained here is well justified. The only possible explanation for the significant green emission enhancement is that the green-emitting levels populate at a rapid rate which cannot be explained through the conventional UC mechanism explained earlier. Here, a new strategic phenomenon is proposed, where there is an energy exchange between two $Er^{3+}$ ions forming an Er–Er ion cluster, the same as the Yb–Yb cooperative energy transfer. At high pump power excitation, the highly populated $^4F_{7/2}$ level becomes saturated and any further energy contribution is transferred to the nearest $^4F_{7/2}$ level of another $Er^{3+}$ ion through the virtual level of a Yb–Yb cluster which leads to the energy bridging between two $Er^{3+}$ ions simultaneously transfer of energy. To investigate more carefully, we have again used a rate equation model for the two neighbouring levels ($^4F_{7/2}$) of two individual $Er^{3+}$ ions that share the same energy transfer populations from a Yb–Yb cluster *via* the cooperative energy transfer model.[5] Here, if we anticipate rapid migration among donors, then the rate equation dynamics of the cooperative transfer upconversion processes can be simplified. Moreover, the migration or energy bridging process can be easily expressed by considering two simultaneous energy transfer processes. The first transfer process takes place from $Er^{3+}$ to $Yb^{3+}$ ($N_{Er,2} \rightarrow N_{Yb,1}$) and the second takes place between $Yb^{3+}$ to $Er^{3+}$($N_{Er,2} \rightarrow N_{Yb,1}$). However, it is to be mentioned that the energy transfer process is *vice versa*. Based on the above assumptions, the rate equation can be expressed as,

$$\frac{dN_{Er,2}}{dt} = \sigma_{abs,Yb}, N_{Yb,1}F - (W_{rad} + W_{nr})N_{Er,2} - KN_{Er}{}^2N_{Yb,1} \quad (9)$$

$$\frac{dN_{Yb,2}}{dt} = -\frac{1}{\tau_a} + KN_{Er}{}^2N_{Yb,1} \quad (10)$$

$$\frac{dN_{Yb,2}}{dt} = \sigma_{abs,Er}, N_{Er,1}F - (W_{rad} + W_{nr})N_{Er,1} - KN_{Yb}{}^2N_{Er,1} \quad (11)$$

$$\frac{dN_{Er,1}}{dt} = -\frac{1}{\tau_a} + KN_{Yb}{}^2N_{Er,1} \quad (12)$$

where $N_{Er,2}$ and $N_{Yb,2}$ correspond to the donor and the acceptor population levels, respectively, involved in the UC process represented by 1st energy transfer. $N_{Yb,2}$ and $N_{Er,1}$ correspond to the donor and the acceptor population levels for the 2nd energy transfer; $\sigma$ is the absorption cross-section of the donor ions; $F$ is the excitation pumping flux; and $K$ is the cooperative energy transfer rate. $W_{rad}$ and $W_{nr}$ represent the radiative and nonradiative losses; $\tau_d = (W_{rad} + W_{nr})^{-1}$ is the experimental decay lifetime of the $^4F_{7/2}$ donor level and $\tau_a$ is the lifetime of the acceptor level.

Under steady state approximation with neglecting transfer term, the population of the acceptor (Yb) level for the 1st transfer process (Er → Yb) and the population of acceptor (Er) level for 2nd transfer process (Yb → Er) can be written as

$$N_{Yb} = N_{Er,1}\tau_a\tau_d{}^2(F\sigma_{abs,Yb})^2N_{Yb,2}N_{Er,2}{}^2 \quad (13)$$

$$N_{Er,1} = N_{Yb,2}\tau_a\tau_d{}^2(F\sigma_{abs,Er})^2N_{Er,2}N_{Yb,2}{}^2 \quad (14)$$

It is worth noticing that eqn (13) demonstrates the predicted quadratic dependency on excitation pump intensity. Moreover, the following equation for energy bridging intensity followed by cooperative-emission may be derived in the steady-state regime from eqn (9) and (11)

$$I_{\text{energy bridging}} = [F\tau_d{}^2(F\sigma_{abs,Yb})^2N_{Er,2}{}^2]_{Er_2\rightarrow Yb_2} + [F\tau_d{}^2(F\sigma_{abs,Er})^2N_{yb,1}{}^2]_{Yb_2\rightarrow Er_1} \quad (15)$$

According to eqn (15), the energy bridging intensity should have a square dependency on the donor concentration; *i.e.*, one part should be dependent on (Er) concentration and another part should depend on (Yb) concentration. Eqn (15) also justifies the idea of energy bridging (population transfer) from one $Er^{3+}$ ion to another $Er^{3+}$ ion and it also provides the idea of the intensity of population transfer at a specific power density. Quantitative analysis (rise time & decay time) on populated levels such as $N_{Er,2}$ will help to decode the energy transfer probability between two $Er^{3+}$ levels *via* the $Yb^{3+}$ virtual level. Eqn (9)–(12) may also be used to estimate the temporal evolution of the whole $Er^{3+}$ upconversion emission process under the rapidly pulsed excitation of the $Yb^{3+}$ ion. It is notable that the cooperative emission capabilities can be greatly enhanced in oxyfluoride glasses,[7,44] fluoride-doped ZBLAN glasses.[17] In some cases, it is found that (5%) Yb-doped oxyfluoride ceramics was 230 times greater than that of ZBLAN fluoride glass doped with $Yb^{3+}$ (3 mol%). The reason for this improvement is that the glass-ceramic composition allows the $Yb^{3+}$ ions to form $Yb^{3+}$/$Yb^{3+}$ clusters directly which is not the case for ZBLAN glasses. The emergence of additional $Yb^{3+}$/$Yb^{3+}$ cluster ions as well as $Yb^{3+}$ and $Er^{3+}$ ion incorporation into the nanocrystalline phase resulted in considerably smaller particle size. In a homogeneous glass, there is less sep-

aration among $Yb^{3+}$ ions. In the present case, the GC865 sample is proven to be a uniquely designed GC matrix as it has a low phonon energy environment of KF, aluminium as the modifier which gives an excellent environment to form $Yb^{3+}$/$Yb^{3+}$ ion pairs at first and then enables clustering of nearby $Er^{3+}$ ions to form the structure $Er^{3+}$–($Yb^{3+}$/$Yb^{3+}$)–$Er^{3+}$ with a neighbouring $Er^{3+}$ ion. This pair proves to be highly efficient in terms of energy mitigation in a higher state. It is a very rare phenomenon where the Er ion at a high pump power not only saturates its $^4F_{7/2}$ level population but also transfers additional energy at a moderately high power through a virtual level of the $Yb^{3+}$/$Yb^{3+}$ ion cluster to the other activator ion. The GC865 sample has the unique advantage of the following improvements: better coupling of the ($Yb^{3+}$/$Yb^{3+}$) ion pairs, less cross-relaxation, non-saturation of the green-emitting levels, population control management at high pump power and a better cooperative upconversion process. In the later section, the photometric characterization of the sample was analysed to check the suitability for low-cost color tuning displays and $Er^{3+}$-doped optical fibres.

**3.3.5 Photometric characterization.** The International Commission on Illumination (CIE) developed the CIE 1931 RGB color space and CIE 1931 XYZ color space in 1931. The CIE color coordinates are the first quantifiable relationships between wavelength distributions in the electromagnetic visible spectrum and physiologically experienced colors in human color vision. To show the actual color from the UC luminescence, the CIE color coordinates for the GC865 sample, different excitation pump powers were calculated. These calculations are using the following formulas:[45]

$$x = \frac{X}{X+Y+Z}, y = \frac{Y}{X+Y+Z} z = \frac{Z}{X+Y+Z} \quad (16)$$

where $Y$ is brightness, $Z$ is quasi-equal to blue (of CIE RGB), and $X$ is a blend of the three CIE RGB curves in the CIE 1931 model, also known as the tristimulus values. The tristimulus values for a color with a spectral power distribution $P(\lambda)$ are given by,

$$X = \int_{400}^{720} P(\lambda)x'(\lambda)\mathrm{d}\lambda$$
$$Y = \int_{400}^{720} P(\lambda)y'(\lambda)\mathrm{d}\lambda \quad (17)$$
$$Z = \int_{400}^{720} P(\lambda)z'(\lambda)\mathrm{d}\lambda$$

where $\lambda$ is the wavelength of the equivalent monochromatic light and $x'(\lambda)$, $y'(\lambda)$ and $z'(\lambda)$ are the three color-matching functions.[45–47] However, the two derived parameters $x$ and $y$ are then used to specify the chromaticity, with two of the three normalized values being functions of the three tristimulus values: $X$, $Y$, and $Z$.

The CIE 1931 chromaticity diagram for the GC865 sample is shown in Fig. 12.

To define the actual color emission, CIE parameters *e.g.* color coordinates ($x$, $y$) and CCT were computed using the Color-Calculator software. It is been observed that the color coordinates traversed a broad range from white to an intense green area, as seen in the chromaticity diagram on the increase of the excitation pump power density (Fig. 13).

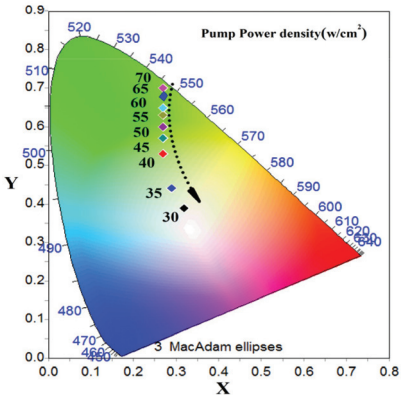


Fig. 12 Color coordinates for various pump power density $Er^{3+}$/$Yb^{3+}$ codoped BAKL glass-ceramics.

The color coordinates ($x$,$y$) are presented in Table 1, which shows that there is a possibility of tuning the color from white to green. Moreover, it is quite interesting; at a moderate power (530 mW), the sample emits white light ($x$ = 0.32, $y$ = 0.39) which is very close to the white centre (0.33, 0.33) of the MacAdam ellipse. In addition, according to the National Television Standard Committee (NTSC) system, the ideal white chromaticity lies near (0.33, 0.33).[48] The bright white-light emission can be easily observed with the naked eye during the test. However, with incremental pump powers, the CIE coordinates show the trend of moving from the white to the green-light regions. The reason behind this occurrence is already justified using the energy bridging phenomenon between the Er–Er ion clusters in the above section. The major advantage of the present material is that by simply adjusting the excitation pump power, the GC865 sample can exhibit tunable visible light, which is why the current sample is expected to have

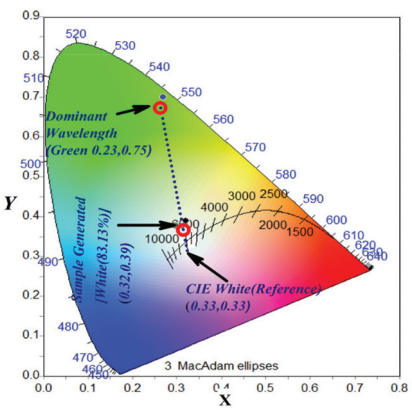


Fig. 13 Color purity calculation diagram in terms of the dominant wavelength.

Table 1 CIE parameters of BAKL:$Er^{3+}$/$Yb^{3+}$ (GC865) ceramic phosphor with different pump power densities

| Ceramic phosphor | Excitation pump power density (W $cm^{-2}$) | Color coordinates | | CCT (K) | Color purity (%) |
|---|---|---|---|---|---|
| | | $x$ | $y$ | | |
| GC865 | 35 | 0.32 | 0.39 | 5130 | 16.88 |
| | 40 | 0.29 | 0.45 | 4526 | 30.67 |
| | 45 | 0.27 | 0.53 | 4409 | 49.31 |
| | 50 | 0.27 | 0.57 | 4515 | 58.24 |
| | 55 | 0.26 | 0.60 | 4447 | 65.32 |
| | 60 | 0.26 | 0.63 | 4509 | 72.03 |
| | 65 | 0.25 | 0.65 | 4431 | 76.88 |
| | 70 | 0.25 | 0.70 | 4526 | 88.06 |

broad application prospects in multicolor displays. It can replace the need for RE concentration-dependent phosphor for display applications. To further study its suitability in commercial phosphor (w-LEDs), the quality of this white light was inspected with the correlated color temperature (CCT). The CCT formula is expressed in the following using McCamy empirical formula,[48]

$$\mathrm{CCT} = 449n^3 + 3525n^2 + 6823n + 5520.33 \quad (18)$$

where $n = (x - x_e)/(y - y_e)$ is the reciprocal slope and ($x_e$ = 0.332, $y_e$ = 0.186) the epicenter of the isotemperature lines. The CCT value of the current phosphor was found to vary from 4409 to 5130 K at varying pump powers as shown in Table 1. Conventionally, the CCT value (<5000 K) indicates the warm white light used for inside home appliances and (>5000 K) indicates cooler white light mostly used in outside display applications.

The CCT value calculated for the GC865 excited at 980 nm was found to be 5130 K, which corresponds to a cooler color temperature and generates bluish-white light. Therefore, the present GC865 ceramic phosphor could be suitable for solid-state lighting technology as a cooler white light source, especially for outside display lights.

Although CCT is an efficient characterization, it is mostly used for broadband light sources (white light). The narrow banded light (inorganic emissions) is characterized usually by the dominant wavelength and color purity. As a consequence, the color purity should be checked in the present case. The color purity is calculated with the help of the color calculator software that uses the equation as follows:[49]

$$\text{Color purity} = \frac{\sqrt{(x_s - x_i)^2 + (y_s - y_i)^2}}{\sqrt{(x_d - x_i)^2 + (y_d - y_i)^2}} \times 100\% \quad (19)$$

where ($x_s$, $y_s$) are the coordinates of a sample point, ($x_d$, $y_d$) are the coordinates of the dominant wavelength, and ($x_i$, $y_i$) are the coordinates of the illuminant point. In this study, ($x_d$, $y_d$) = (0.23, 0.75) and ($x_i$, $y_i$) = (0.3101, 0.3162) (illuminants C) for the dominant wavelength at 545 nm are shown in Fig. 10. The calculation was carried out as per ref. 49. The calculated results are shown in Table 1 and indicate that the color purity increased with the pump power dependence. As a result of altering the pump power of the 980 nm excitation, the color purity was enhanced to 88.06%. Commercially white LEDs are fabricated with yellow phosphor-coated blue LEDs[50] and direct white emission is very rare to be found, in particular, in the case of RE doped phosphor. These results show that with efficient doping of $Er^{3+}$/$Yb^{3+}$ in the BAKL host, great tunability from white to intense green emission can be achieved with almost ideal white chromaticity and intense green with high color purity using an NIR excitation source.

## 4. Conclusions

Uniquely designed lithium aluminate fluoroborate glass-ceramics were synthesized and made optically active with the incorporation of $Er^{3+}$/$Yb^{3+}$ ions. Structural characterization, *e.g.* TGA, XRD, and FTIR, confirmed the nucleation and formation of the proposed glass-ceramics. Optical absorption near 979 nm through DRS confirmed the possibility of showing UC luminescence in the GC865 sample. $Er^{3+}$ characteristic bands, such as 525, 555 and 656 nm, were observed well in the UC emission spectra. Due to the use of optimized dopant concentrations and a supportive low phonon energy environment from the host, intense green emission was observed. Interesting results were observed when the excitation pump power was varied from moderate to high powers. The sample emitted white light at moderate low power with almost ideal white chromaticity with an analogy to the NTSC standards. The green emission intensity has significantly increased in comparison to other wavelengths at the high excitation pump power and the anomalous behaviour is explained using the rate equation modelling for the Er–Er energy transfer from the $^4F_{7/2}$ level. The UC mechanism used to elaborate the results is new to the best of our knowledge and can be used to explain a strategic UC mechanism that defect-state luminescence fails to justify. The CIE parameters show that the emitted white light can be used as a cooler white light source due to its observed high CCT value (~5130 K). Wide color tunability from the current phosphor marks its suitability in the field of $Er^{3+}$-doped glass fibre amplifiers and in-display devices with high color purity (88.06%).

## Author contributions

The original design, idea, conceptualization of the work, experiments, data analysis and interpretation and drafting of the article were done by PPS. Visualization and scientific help were provided by KK. Critical review and editing were done by HS.

## Conflicts of interest

The authors have no conflicts of interest to declare. All co-authors have seen and agree with the contents of the manuscript and there is no financial interest to report. We certify that the submission is original work and is not under review at any other publication.

## Acknowledgements

The authors express their sincere thanks to the South African Research Chairs Initiative of the Department of Science and Technology and the National Research Foundation of South Africa (84415). K. Kumar thankfully acknowledges DST-SERB, New Delhi (India) for the financial support [DST (SERB)/EMR/2017/000228]. The financial assistance from the University of the Free State, South Africa is highly recognized. The authors are also thankful to Dr Manoj Kumar Mahata for helping in the analysis of the rate equation modelling.

## Notes and references

1 S. K. Taherunnisa, D. V. K. Reddy, T. SambasivaRao, K. S. Rudramamba, Y. A. Zhydachevskyy, A. Suchocki, M. Piasecki and M. R. Reddy, *Opt. Mater.: X*, 2019, **3**, 100034.
2 H. Ding, L. Lu, Z. Shi, D. Wang, L. Li, X. Li, Y. Ren, C. Liu, D. Cheng, H. Kim, N. C. Giebink, X. Wang, L. Yin, L. Zhao, M. Luo and X. Sheng, *Proc. Natl. Acad. Sci. U. S. A.*, 2018, **115**, 6632–6637.
3 S. Xie, C. Tong, H. Tan, N. Li, L. Gong, J. Xu, L. Xu and C. Zhang, *Mater. Chem. Front.*, 2018, **2**, 1997–2005.
4 S. K. Nam, K. Kim, J.-H. Kang and J. H. Moon, *Nanoscale*, 2020, **12**, 17265–17271.
5 P. P. Sukul, M. K. Mahata, U. K. Ghorai and K. Kumar, *Spectrochim. Acta, Part A*, 2019, **212**, 78–87.
6 Y. Wang and J. Ohwaki, *Appl. Phys. Lett.*, 1993, **63**, 3268–3270.
7 X. Zhang, L. Hu and J. Ren, *J. Phys. Chem. C*, 2020, **124**, 1594–1608.
8 Y. Li, W. Wang, Y. Pan, H. Chen, Q. Cao and X. Wei, *CrystEngComm*, 2020, **22**, 6302–6309.
9 Q. Liu, Y. Tian, C. Wang, F. Huang, X. Jing, J. Zhang, X. Zhang and S. Xu, *Phys. Chem. Chem. Phys.*, 2017, **19**, 29833–29839.
10 Y. K. Kshetri, B. Joshi, T.-H. Kim and S. W. Lee, *J. Mater. Chem. C*, 2017, **5**, 3542–3552.
11 T. Berthier, V. M. Fokin and E. D. Zanotto, *J. Non-Cryst. Solids*, 2008, **354**, 1721–1730.
12 X. Miao, Z. Bai, X. Huo, M. Guo, F. Cheng and M. Zhang, *Ceram. Int.*, 2019, **45**, 8510–8517.
13 F. Steudel, S. Loos, B. Ahrens and S. Schweizer, *J. Lumin.*, 2016, **170**, 770–777.
14 N. Sharmin, M. S. Hasan, A. J. Parsons, D. Furniss, C. A. Scotchford, I. Ahmed and C. D. Rudd, *BioMed Res. Int.*, 2013, **2013**, 902427.
15 B. Xu, D. Tan, S. Zhou, Z. Hong, K. N. Sharafudeen and J. Qiu, *Opt. Express*, 2012, **20**, 29105–29111.
16 J. Yu, L. Hu, Y. Shen and J. Ren, *Inorg. Chem.*, 2021, **60**, 5868–5881.
17 S. V. Adichtchev, V. K. Malinovsky, L. N. Ignatieva, E. B. Merkulov and N. V. Surovtsev, *J. Chem. Phys.*, 2014, **140**, 184508.
18 M. Rodríguez Chialanza, J. F. Schneider, R. Keuchkerian, M. Romero, R. Faccio, A. Olivera and H. Bentos Pereira, *J. Am. Ceram. Soc.*, 2020, **103**, 3126–3137.
19 L. Dimitrocenko, U. Rogulis, A. Veispals, M. Springis, P. Kulis, A. Fedotovs and A. Mishnev, *Phys. Status Solidi C*, 2007, **4**, 753–756.
20 B. Karmakar, Functional bulk metallic glasses, in *Functional Glasses and Glass-Ceramics Processing, Properties and Applications*, Butterworth-Heinemann an impring of Elsevier, 2017, ch. 12, pp. 365–390.
21 G. V. S. Sastry, S. Lele and P. Ramachandrarao, *Rapidly Quenched Met.*, 1984, 1, 177–181.
22 P. P. Sukul and K. Kumar, *Mater. Res. Express*, 2016, **3**, 076207.
23 M. Rodríguez Chialanza, R. Keuchkerian, L. J. Q. Maia, J. F. Carvalho, L. Suescun, R. Faccio and L. Fornaro, *J. Mater. Sci.: Mater. Electron.*, 2018, **29**, 5472–5479.
24 A. Sarakovskis, L. Dimitrocenko, A. Misnevs, U. Rogulis and M. Springis, *J. Phys.: Conf. Ser.*, 2007, **93**, 12041.
25 L. R. Pinckney, Glass-Ceramics, in *Encyclopedia of Physical Science and Technology*, ed. R. A. Meyers, Academic Press, New York, 3rd edn, 2003, pp. 807–816.
26 I. O. Isabella, Optical Properties of Borate Glass-Ceramics, *Dissertation zur Erlangung des Grades Doktor der Naturwissenschaften genehmigt vom Fachbereich Physik der Universitat Osnabruck*, 2005, pp. 1–114.
27 C. Gautam, A. K. Yadav and A. K. Singh, *ISRN Ceram.*, 2012, **2012**, 428497.
28 M. L. F. Nascimento, L. A. Souza, E. B. Ferreira and E. D. Zanotto, *J. Non-Cryst. Solids*, 2005, **351**, 3296–3308.
29 A. Rafferty, R. G. Hill and D. Wood, *J. Mater. Sci.*, 2003, **38**, 2311–2319.
30 S. Zhang, J. Wu, Q. Yang, R. Tu, C. Wang, Q. Shen and L. Zhang, *AIP Adv.*, 2015, **5**, 47125.
31 A. C. Wright, *Int. J. Appl. Glass Sci.*, 2015, **6**, 45–63.
32 A. P. Howes, N. M. Vedishcheva, A. Samoson, J. V. Hanna, M. E. Smith, D. Holland and R. Dupree, *Phys. Chem. Chem. Phys.*, 2011, **13**, 11919–11928.
33 V. Dracopoulos, B. Gilbert and G. N. Papatheodorou, *J. Chem. Soc., Faraday Trans.*, 1998, **94**, 2601–2604.

 

34 Y. Han, C. Gao, S. Li and Z. Jiang, *J. Alloys Compd.*, 2020, **838**, 155610.
35 P. P. Sukul and K. Kumar, Photoluminescence study of $Yb^{3+}/Er^{3+}$ co-doped $Sb_2O_3$-$WO_3$-$Li_2O$ (SWL) ceramic phosphor for fingerprint detection in forensic science and security writin, *Proc. SPIE 10801, Optical Materials and Biomaterials in Security and Defence Systems Technology XV*, 2018, 108010E.
36 P. P. Sukul and K. Kumar, *J. Lumin.*, 2017, **185**, 92–98.
37 L. I. Shanfeng, Z. Min, P. Yang, Z. Qingyu and Z. Mingshan, *J. Rare Earths*, 2010, **28**, 237–242.
38 B. Golesorkhi, A. Fürstenberg, H. Nozary and C. Piguet, *Chem. Sci.*, 2019, **10**, 6876–6885.
39 J. F. Philipps, T. Töpfer, H. Ebendorff-Heidepriem, D. Ehrt and R. Sauerbrey, *Appl. Phys. B*, 2001, **72**, 399–405.
40 M. K. Mahata, T. Koppe, T. Mondal, C. Brüsewitz, K. Kumar, V. Kumar Rai, H. Hofsäss and U. Vetter, *Phys. Chem. Chem. Phys.*, 2015, **17**, 20741–20753.
41 H. Ebendorff-Heidepriem and D. Ehrt, *Glass Science and Technology-Glastechnische Berichte*, 1998, **71**, 289–299.
42 B.-C. Hwang, S. Jiang, T. Luo, J. Watson, G. Sorbello and N. Peyghambarian, *J. Opt. Soc. Am. B*, 2000, **17**, 833–839.
43 J. Zhang, Z. Hao, J. Li, X. Zhang, Y. Luo and G. Pan, *Light: Sci. Appl.*, 2015, **4**, e239–e239.
44 D. Deng, S. Xu, R. Bao, S. Zhao, B. Wang, H. Wang and H. Ju, *J. Phys. D: Appl. Phys.*, 2009, **42**, 105111.
45 T. M. Goodman, *Colour Des. Theor. Appl. Second Ed.*, 2012, 417–452.
46 M. Bertalmío, *Vis. Model. High Dyn. Range Wide Colour Gamut Imaging*, 2020, pp. 131–155.
47 Color Matching Function - an overview | ScienceDirect Topics, https://www.sciencedirect.com/topics/engineering/color-matching-function, (accessed 24 September 2021).
48 M. Sato, S. W. Kim, Y. Shimomura, T. Hasegawa, K. Toda and G. Adachi, *Handb. Phys. Chem. Rare Earths*, 2016, vol. 49, pp. 1–128.
49 http//www.madebydelta.com/imported/images/documents/ICAM/I103%20Dominant%20Wavelength.pdf Domin. Wavel. Color purity Emit. Color.
50 Y. N. Ahn, K. Do Kim, G. Anoop, G. S. Kim and J. S. Yoo, *Sci. Rep.*, 2019, **9**, 16848.